International Journal of Heat and Mass Transfer 136 (2019) 1006–1016

Contents lists available at ScienceDirect

International Journal of Heat and Mass Transfer

journal homepage: www.elsevier.com/locate/ijhmt

Anisotropic corrections for the downwelling radiative heat transfer flux from various types of aerosols

Zhouyi Liao, Mengying Li, Carlos F. M. Coimbra *

Department of Mechanical and Aerospace Engineering and Center for Energy Research, University of California San Diego, 9500 Gilman Drive, La Jolla, CA 92093, USA

ARTICLE INFO

Article history:
Received 26 November 2018
Received in revised form 1 March 2019
Accepted 5 March 2019

Keywords:
Aerosol anisotropic scattering
Mie theory
Monte Carlo method
δ-M approximation
Net result-based scaling

ABSTRACT

Comprehensive Monte Carlo simulations are used to correct deviations in the atmospheric downwelling longwave (DLW) radiative flux calculated by isotropic scattering assumptions. The widely used δ-M approximation is validated for low to medium values of aerosol loading. For very high aerosol loading conditions, the δ-M approximation incurs an error. Here we propose scaling corrections for extreme loading conditions routinely found in selected urban areas in Asia, but also in other continental and coastal areas susceptible to large-scale wildfire pollution (Western USA) or dust storms (Mediterranean regions and Northern Africa). The scaling rules are expressed as functions of the normalized aerosol optical depth t^* and the scattering asymmetry factor e_g. An exponential relationship between the DLW deviation that assumes isotropic scattering and t^* is found, and the corresponding fitting coefficients are correlated for different types of aerosols (sample internal mixing, urban, continental and marine aerosols). The δ-M approximation is sufficiently accurate when aerosol optical depths (AOD) at the ground level are smaller than 0.5. For AOD beyond this threshold, the proposed scaling rule corrections should be used for estimation of downwelling thermal radiative fluxes. The effects of moisture content on aerosol composition and on DLW radiative fluxes are also investigated for all conditions of interest.

1. Introduction

The accurate determination of downwelling longwave (DLW) radiation, also referred as sky or atmospheric radiosity, is critically important to many engineering, meteorological and agricultural applications. These applications include the balance of heat and mass fluxes for cooling towers and power plants, the calculation of surface evaporative fluxes from vegetation and outdoor equipment, and many other engineering applications, both in urban and natural settings [1,2]. Related concepts, such as the 'effective sky temperature' or the 'effective sky emissivity' also provide physical insight on the operation of meteorological and radiometric instruments, as well as on the performance of passive cooling devices [3,4].

Atmospheric downwelling radiation within the range of 4–100 μm can be measured directly by infrared pyrgeometers, which are more expensive and more difficult to calibrate due to ground interference than the pyranometers commonly used for shortwave radiation [1,5]. Therefore, widespread experimental determination of DLW is often hindered by both capital and maintenance costs associated with infrared telemetry. Also, well-maintained pyrgeometers are only found in a small fraction of existing meteorological stations, and therefore real-time values of sky radiosity are not available with sufficient spatial resolution to be useful for thermal management of industrial equipment. Remote sensing offers an alternative for indirect calculation of atmospheric radiosity, but again, the relatively low temporal and spatial resolutions currently available are limiting for practical purposes and real-time applications [6].

Theoretical determination of DLW for cloudless (clear) skies is possible by a combination of atmospheric temperature and concentration profiles, high resolution absorption data for the main gas constituents of the atmosphere, and radiative transfer models that incorporate these high spectral resolution data sets into line-by-line calculations [7]. Radiative transfer in diffuse (isotropic) media can be modeled accurately using a two-flux approach to minimize computational resources because the absorption, emission and scattering of longwave radiation by gases in the atmosphere can be closely modeled as diffuse [7]. However, the scattering of longwave radiation by real aerosols can diverge substantially from isotropic behaviour.

It is well-known that the Monte Carlo method offers a relatively simple way to model the radiative transfer problem in the atmosphere with high levels of physical realism, including complex

* Corresponding author.
E-mail address: ccoimbra@ucsd.edu (C.F.M. Coimbra).

https://doi.org/10.1016/j.ijheatmasstransfer.2019.03.031
0017-9310/

effects of anisotropy and polarization. Here we use an anisotropic Mie scattering formulation to model the contributions to DLW caused by aerosols, and compare those solutions to the line-by-line results obtained by the isotropic scattering assumption. This comparison allows us to develop corrective scaling rules for the fluxes that is applicable to different aerosol types and a wider range of aerosol loading values.

When anisotropic effects are taken into account, scaling methods are employed to scale the anisotropic effects into an isotropic scattering formulation [8]. Most of the scaling methods previously proposed are based on the transformation of optical depth and the phase function [9]. The works by Joseph et al. [10] and Potter [11] used δ-distribution approximations for the forward peaks of the aerosol scattering phase functions. Wiscombe extended the δ-distribution approximation to develop what is now called the δ-M approximation [12]. Lee and Buckius further developed several scaling methods for P-1 approximations and two-flux methods [8]. Some of these scaling techniques were compared with exact solutions [8,13], or with Monte Carlo (MC) simulations [14,15], and were validated for specific conditions. Lee and Buckius compared the heat flux simulated with $a_1/3$ scaling (derived from P-1 scaling) and with $2f1$ scaling with exact solutions to obtain fairly accurate results [8]. Guo and Maruyama [13] conducted similar comparisons between the results simulated from scaling techniques based on δ-distribution approximations versus results obtained with anisotropic scattering computations. For more complex anisotropic scattering problems, integrated P-1 and MC simulations are compared to pure MC simulations, and the former is (not surprisingly) found to be faster but less accurate [14].

Although the studies above have exploited the validity of various scaling techniques, those calculations were conducted for relatively low aerosol loading (e.g. low aerosol concentrations). Moreover, the spectral variability and the sensitivity to asymmetry factors for different aerosol types were not considered in previous studies. The present study employs complete Monte Carlo simulations to analyze the validity of the -M approximation for all practical values of aerosol optical depths (AODs). We also propose corrections to the -M approximation when large deviations are observed for high AOD values.

Symbols used throughout the paper are listed in Table 1. The following Section 2 presents an overview of the longwave radiative model adopted in this work. Section 3 presents the details about the Monte Carlo methods used to develop the scaling rules. Section 4 presents the resulting scaling rules for different types of aerosols and high AOD values. Conclusions follow in Section 5.

Table 1
Nomenclature and Abbreviations.

Symbol	Explanation
Nomenclature	
$D(t^*)$	The anisotropic correction factor that quantifies the anisotropic scattering effect
e_g	Asymmetry factor
$I(\kappa, \mu)$	Radiant intensity in the medium, W m^{-2} sr^{-1}
I_b	Blackbody radiant intensity, W m^{-2} sr^{-1}
I_ν	Spectral radiant intensity per unit of wavenumber ν, W cm m^{-2} sr^{-1}
j_ν	Source function that represents photon emission and scattering
L	Thickness of the atmosphere, m
$P(\cos\Theta, e_g)$	Scattering phase function
q^-_{ani}	Downwelling longwave radiative flux in anisotropic case, W m^{-2}
q^-_{iso}	Downwelling longwave radiative flux in isotropic case, W m^{-2}
s	physical path length, m
T	Temperature, K
t^*	Normalized aerosol optical depth, $\kappa_s L/\kappa_{s0} L$
κ	Absorption (κ_a), scattering (κ_s) or extinction (κ_e) coefficients, cm^{-1}
μ	Zenith direction of the radiation ray, $\cos(\theta)$
μ'	Scattered zenith direction of radiation ray, $\cos(\Theta)$
ξ	Random number sampled uniformly from 0 to 1
$\tilde{\rho}$	Single scattering albedo
τ	Optical depth
Φ	Scattering azimuth angle with respect to incident ray, rad
ϕ	Azimuth angle, rad
ϕ_r	Particle growth factor
Θ	Scattering zenith angle with respect to incident ray, rad
θ	Zenith angle, rad
Abbreviations	
AOD	Aerosol optical depth at 500 nm
DLW	Downwelling longwave radiative flux, W m^{-2}
HG	Henyey-Greenstein phase function
MC	Monte Carlo simulation
MCRT	Monte Carlo Radiative Transfer
MSB	multi-spectral Energy Bundle Method
RTE	Radiative Transfer Equation

2. Overview of the longwave radiative model

2.1. A model atmosphere

The cloud-free atmosphere is modeled by 18 plane-parallel layers as shown in Fig. 1. The pressure of each layer is determined by a constant σ coordinate system as proposed in [7,16]. The AFGL mid-latitude summer profile is used for temperature and pressure profiles as well as for the vertical profiles of seven participating atmospheric gases: water vapor, carbon dioxide, ozone, methane, nitrous oxide, oxygen and nitrogen [17]. The vertical profiles of gases are corrected by their current surface concentrations [7]. The layer averaged temperature and constituent concentrations are averaged using pressure values as the weights [7,16]. The altitude of layer boundary and average temperature in each layer is shown in Fig. 1. The gaseous absorption coefficients are calculated using the most up-to-date HITRAN molecular spectral data for these seven gases [18]. All gases are assumed to be purely absorbing in the longwave spectrum without any scattering effects [19]. The vertical aerosol optical depth profile is adopted from [20] using the Cloud Aerosol LIDAR and Infrared Pathfinder Satellite Observations (CALIPSO) over North America.

2.2. The optical properties of aerosols

The absorption, scattering coefficients and asymmetry factor of aerosols are calculated using Mie theory from the size distribution and refractive index of aerosol particles [21], which are dependent on their physical and chemical compositions. Common aerosol components include water-soluble salts, soots, dusts and water droplets. The composition of aerosols varies from region to region with each component having typical size distributions and refractive indexes. Finer particles (such as industrial soot) are normally anthropogenic in origin and mostly found in urban areas [22]; marine aerosols are mostly water droplets generated by wave and tide motion; continental aerosols are composed mostly by dust [21]. Four types of aerosols are considered in this work: the internal mixing aerosols from Refs. [7,23], maritime aerosols, continental aerosols and urban aerosols. The compositions (volume fractions, %) of the latter three aerosol types are presented in Table 2 (for dry aerosols). The values inside the brackets are number fractions (%) [21].

In-situ observations have shown that log-normal distribution are appropriate to describe aerosol size distributions [27,28]. The mixture size distribution is the summation of the distribution functions of each component. For dry aerosols, the size distribution follows

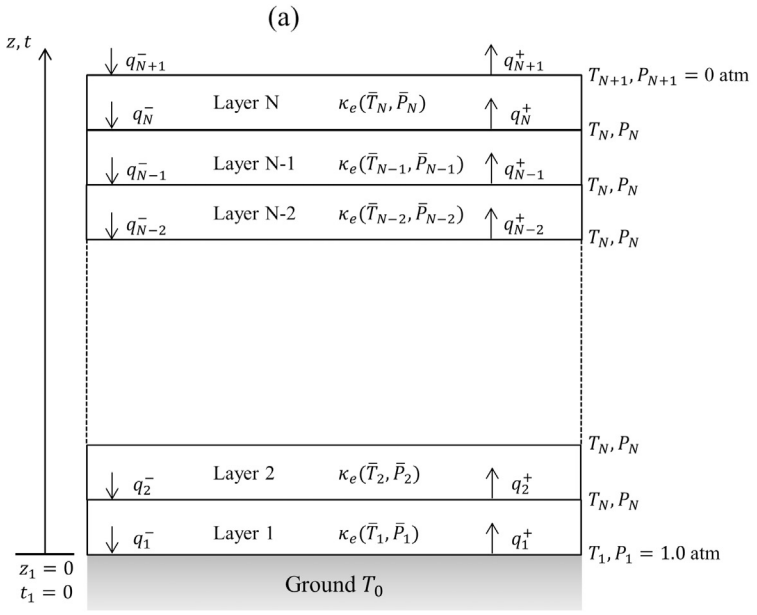

(b)

N	Upper boundary z_N(m)	Average T_N(K)
18	120,000	274.9
17	32,700	230.1
16	23,500	220.1
15	18,500	216.5
14	15,100	217.2
13	12,600	225.6
12	10,500	238.3
11	8,640	249.3
10	7,050	258.8
9	5,700	266.7
8	4,490	273.4
7	3,450	279.2
6	2,550	284.0
5	1,790	287.6
4	1,160	290.1
3	664	292.0
2	300	293.4
1	68	294.0
Ground	0	294.2

Fig. 1. (a) Schematic representation of the multilayer model of the Earth-atmosphere system with a total of N atmosphere layers. Altitude and optical depth are labeled as z and t, respectively; (b) Altitude of layer boundaries and layer-averaged temperatures.

Table 2
The volume fraction (%) of the four basic components for three aerosol types (the numbers inside the brackets are the number fractions (%)) [24–26].

Aerosol Type	Dust-like (DL)	Water-Soluble (WS)	Oceanic (OC)	Soot (SO)
Maritime		5 (99.96)	95 (0.04)	
Continental	70 (0.02)	29 (93.83)		1 (6.16)
Urban	17 (1.65×10^{-5})	61 (59.25)		22 (40.75)

$$\frac{dn(r)}{dr} = \sum_{i=1}^{I} \frac{N_i}{\sqrt{2\pi} r \ln \sigma_i} \exp\left[-\frac{1}{2}\left(\frac{\ln r - \ln r_{m,i}}{\ln \sigma_i}\right)^2\right], \quad (1)$$

where $r_{m,i}$ (μm) is the mode radius, σ_i (μm) measures the width of the distribution, and N_i (number/cm^3) is the particle number density of component i. The distribution characteristics of the four basic components are listed in Table 3 [26]. Complex refractive indices for the dry components are tabulated in [23].

Ambient relative humidity are found to have an effect on the optical properties of aerosols since the refractive index and size of aerosols are changed if water vapor is being absorbed. To consider the effects of relative humidity, the equivalent complex refractive index for wet aerosols can be estimated using the particle growth factor ϕ_r [29],

$$n = n_0 \phi_r^{-3} + n_w\left[1 - \phi_r^{-3}\right] \quad (2)$$

$$k = k_0 \phi_r^{-3} + k_w\left[1 - \phi_r^{-3}\right] \quad (3)$$

where the subscript '0' indicates dry aerosols and the subscript 'w' indicates liquid water. The mode radius for wet aerosols are those for dry aerosols times the growth factor. Growth factors for both refractive indices and radius are listed in Table 4.

If AOD at 500 nm is specified, with the scale height for the troposphere to be 1575 m [7], the aerosol extinction coefficient at 500 nm is $\kappa_{e@500nm} = \mathrm{AOD}/\bar{L}$. Then the particle number density of each component can be inferred from the specified AOD, as described in [7]. Fig. 2 shows the spectral absorption and scattering coefficients and asymmetry factors for different types of aerosols when AOD is 0.1 and RH is 70%. Marine aerosols have the highest asymmetry factor over the entire longwave spectrum, followed by continental aerosols and urban aerosols.

The scattering diagrams presented in Fig. 3 illustrate how the incident radiation is scattered for various asymmetry factors. When the asymmetry factor is positive, forward scattering is favored and when the asymmetry factor is negative, backward scattering is more likely to occur.

2.3. Input scaling by δ-M approximation

One approach to correct the anisotropic scattering effect is to scale the input optical properties to an isotropic scattering medium. Several approximation methods are available. Among them, the δ-M approximation derived by scaling the radiative transfer equation yields the best results when comparing to exact solutions [8]. In this case, the extinction coefficient and single scattering albedo are scaled as,

$$\hat{\kappa} = (1 - \tilde{\rho} e_g)\kappa$$
$$\hat{\tilde{\rho}} = \frac{\tilde{\rho}(1 - e_g)}{(1 - \tilde{\rho} e_g)} \quad (4)$$

where e_g is the asymmetry factor of the real phase function. After scaling, the phase function is replaced by $P(\cos\Theta) = 1$ and the

Table 3
Microphysical characteristics of the four basic components in dry conditions [26].

component	Dust-like (DL)	Water-Soluble (WS)	Oceanic (OC)	Soot (SO)
$r_{m,i}$, μm	1.000	0.010	0.600	0.024
σ_i, μm	2.990	2.990	2.510	2.000

Table 4
Growth factors used to adjust particle size distributions and refractive index [26,30].

Relative humidity	30%	40%	50%	60%	70%	80%	90%
Constituent	Growth factor for Relative Humidity						
Dust-like (DL)	1.000	1.000	1.000	1.000	1.000	1.000	1.000
Water-Soluble (WS)	1.000	1.000	1.573	1.620	1.790	1.965	2.345
Oceanic (OC)	1.000	1.000	1.000	1.000	1.000	1.000	1.000
Soot (SO)	1.000	1.000	1.000	1.016	1.033	1.186	1.407

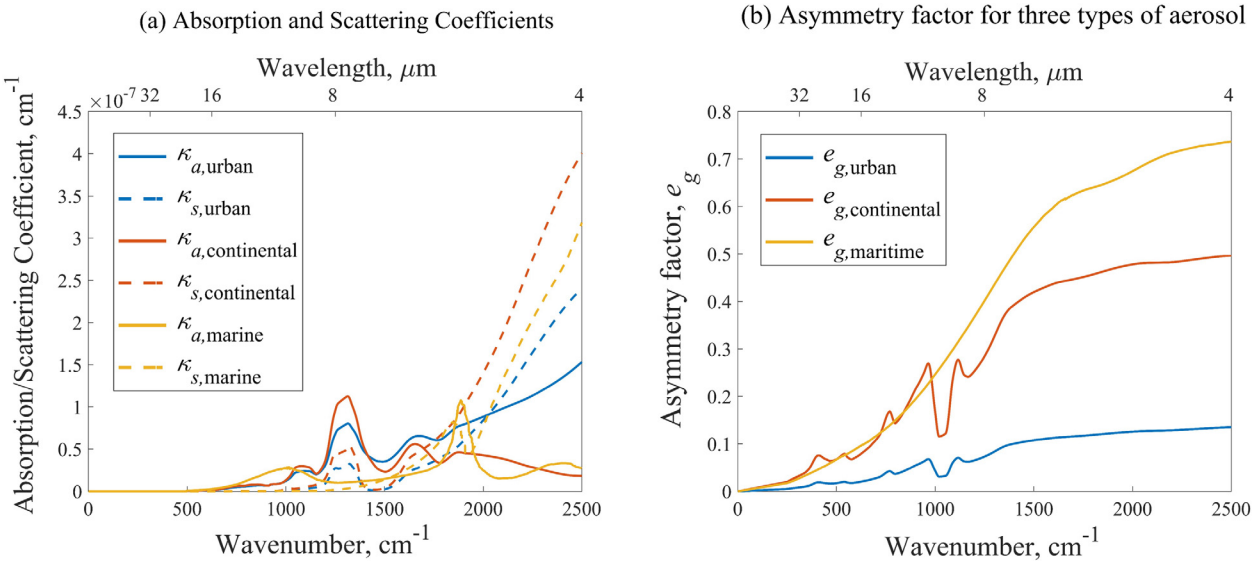

Fig. 2. Spectral (a) absorption and scattering coefficients and (b) asymmetry factors of urban, continental and marine aerosols when AOD = 0.1 and RH = 70%.

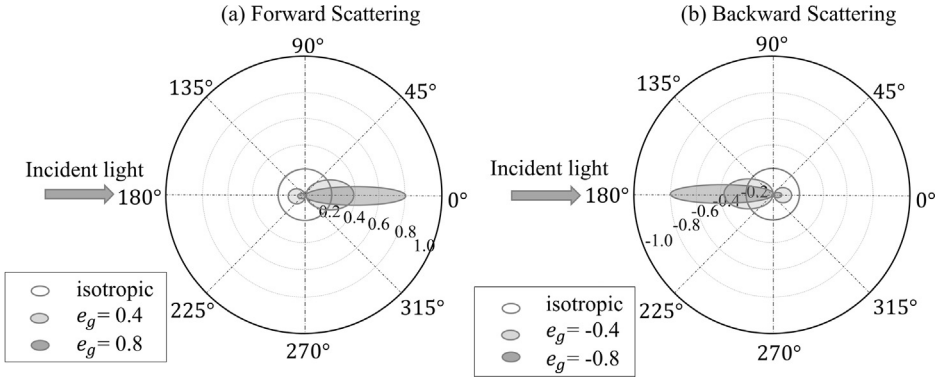

Fig. 3. Scatter diagram of scattering phase functions for forward and backward scattering with various asymmetry factors.

extinction coefficient and single scattering albedo are replaced by $\hat{\kappa}$ and $\hat{\rho}$, respectively. Following this procedure, anisotropic scattering problems can be approximated and treated as isotropic scattering problems.

Different from scaling the input parameters, another approach is to scale the net result. Scaling rules for this approach will be derived in Section 4.

3. The Monte Carlo method

Monte Carlo (MC) methods offer statistical means for studying stochastic physical processes (emission, absorption and scattering of bundles of radiant energy or photons) by a large number of simulations. Here the MC algorithm is used to compute the upwelling and downwelling longwave fluxes across each boundary, with longwave radiation emitted both by the ground and the atmosphere.

3.1. Photon emission

Emitting sources in Monte Carlo Radiative Transfer (MCRT) simulation can be divided into two classes: directional point source or diffuse emission, where the latter is the case of longwave emission in the atmosphere [31]. The energy contained in each diffusely emitted photon bundle depends on the total emissive power E_{bs} for a surface or E_{bg} for a gas layer, as well as the number of bundles N [32],

$$E_{bs} = \varepsilon \sigma T_s^4, \tag{5}$$

$$E_{bg} = 4\kappa_a \Delta z \int_{\Delta v} I_{bv}(T_g)dv, \tag{6}$$

where

$$I_{bv}(T_g) = \frac{2hc^2v^3}{e^{hcv/(k_BT_g)} - 1} \tag{7}$$

represents the wavenumber v-based Planck distribution, $\sigma = 5.67 \times 10^{-8}$ W m^{-2} K^{-4} is the Stefan-Boltzmann constant; ε is the surface emittance; κ_a (cm^{-1}) is the absorption coefficient of the gas volume; Δz (m) is the thickness of the atmospheric layer; $h = 6.626 \times 10^{-34}$ J s is Planck's constant and $k_B = 1.38 \times 10^{-23}$ J K^{-1} is the Boltzmann constant.

The location of photon emission is randomly sampled across surfaces and volumes. For a photon bundle emitted from a surface, the zenith angle θ (in the range of 0 to $\pi/2$) and the azimuth angle ϕ are sampled as [33]:

$$\theta = \cos^{-1}\left(\sqrt{\xi_\theta}\right), \qquad \phi = 2\pi\xi_\phi. \tag{8}$$

For a photon bundle emitted from a volume of gas, the range of its zenith angle is extended to $[0, \pi]$,

$$\theta = \cos^{-1}(2\xi_\theta - 1), \qquad \phi = 2\pi\xi_\phi, \tag{9}$$

where ξ_ϕ and ξ_θ are random numbers uniformly sampled from 0 to 1.

3.2. Collision-based Monte Carlo approach

The Monte Carlo simulation procedure for forward collision-based approach is illustrated in Fig. 4. An emitted photon bundle is assumed to travel undisturbed until it collides with a molecule or a particle, where it is either absorbed or scattered.

The probability that a photon bundle travels an optical depth τ without collision is:

$$p(\tau)d\tau = e^{-\tau}d\tau. \tag{10}$$

Then the traveled optical depth before next collision is sampled as [34,35]

$$\begin{aligned} \xi_\tau &= \int_0^{\tau_0} e^{-\tau}d\tau = 1 - e^{-\tau_0}, \\ \tau_0 &= -\ln(1-\xi_\tau) = -\ln\xi_\tau. \end{aligned} \tag{11}$$

The physical distance traveled between consecutive collisions is

$$d_c = \frac{\tau_0}{\kappa_v} = -\frac{\ln\xi_\tau}{\kappa_e}, \tag{12}$$

where ξ_τ is the sampled random number, κ_e (cm^{-1}) is the extinction coefficient of current medium.

After determining d_c, the distance to the nearest boundary d_b (m) along the direction of propagation is calculated. Then d_b and d_c are compared to determine whether the collision occurs in the current layer, or after crossing the boundary. If $d_c < d_b$, the collision occurs in the current layer and the photon may either be absorbed or scattered. The probability of scattering is determined by the single scattering albedo of the medium. If absorbed, the energy of the photon bundle is converted to the thermal field of the media. If scattering occurs, the bundle is traveling in a new direction determined by the scattering angle, which is sampled by inverting the Henyey-Greenstein scattering phase function [36],

$$\begin{aligned} P_{\mathrm{HG}}(\cos\Theta, e_g) &= \frac{1-e_g^2}{2\left[1+e_g^2-2e_g(\cos\Theta)\right]^{3/2}}, \\ \cos\Theta &= \frac{1}{2e_g}\left\{1 + e_g^2 - \left[\frac{1-e_g^2}{1-e_g+2e_g\,\xi_\Theta}\right]^2\right\}, \\ \Phi &= 2\pi\xi_\Phi. \end{aligned} \tag{13}$$

Then, a new scattering direction (r'_x, r'_y, r'_z) is generated according to the incoming ray direction (r_x, r_y, r_z) and the scattering angles [37]

$$\begin{aligned} r'_x &= r_x\cos\Theta - \tfrac{\sin\Theta}{\sqrt{1-r_z^2}}\left(r_x r_z\cos\Phi + r_y\sin\Phi\right), \\ r'_y &= r_y\cos\Theta - \tfrac{\sin\Theta}{\sqrt{1-r_z^2}}\left(r_y r_z\cos\Phi - r_x\sin\Phi\right), \\ r'_z &= r_z\cos\Theta + \sqrt{1-r_z^2}\sin\Theta\cos\Phi. \end{aligned} \tag{14}$$

If $d_c > d_b$, the photon is advanced to the boundary and its coordinates are updated accordingly,

$$x' = x + r_x d_b, \qquad y' = y + r_y d_b, \qquad z' = z + r_z d_b. \tag{15}$$

If the boundary is an external boundary, the energy contained in this photon bundle is recorded as an outgoing energy flux or energy absorbed by a surface. If the external surface is non-black, the possible reflection should also be considered. If an internal boundary is crossed, energy flux to the next layer is recorded. Moreover, d_c and d_b are also updated according to the optical properties in the new layer. The remaining distance to collision is then

$$d'_c = \frac{\kappa_v}{\kappa'_v}(d_c - d_b), \tag{16}$$

where κ'_v (cm^{-1}) is the extinction coefficient in the just-entered layer. The updated distance to collision d'_c and distance from the updated position to next boundary d'_b are compared. This process continues until the bundle is absorbed or exits the external boundaries [38].

3.3. Computational performance

The Multi-Spectral Energy Bundle (MSB) method is used to reduce the computational cost associated with the line-by-line Monte Carlo simulations [39]. The MSB method treats the energy bundles as multi-spectral rays composed of a set of sub-bundles in order to make the spectral integration more efficient. Unlike the energy emitted by each monochromatic bundle represented by Eqs. (5) and (6), the averaged energy of a photon bundle is

$$E_{bg} = \int_V \int_{4\pi} \int_0^\infty \kappa_v I_{bv} dv d\Omega dV = 4\pi V \int_0^\infty \kappa_v I_{bv} dv, \tag{17}$$

where κ_v (cm^{-1}) is the spectral absorption coefficient, v (cm^{-1}) is the wavenumber and I_{bv} (W m^{-2}) is the blackbody spectral intensity given by the Planck distribution. In the MSB approach, the bundles are composed by a set of sub-bundles, each carrying a certain amount of energy and having a specific wavenumber. The energy of the multi-spectral bundle will be the summation of the energy of its sub-bundles [39]. The longwave spectral range (0–2500 cm^{-1}) with a resolution of 0.01 cm^{-1} is uniformly divided into N_b sub-bands with respect to wavenumber, each with a specific Planck-mean absorption, scattering coefficients and single scattering albedo

$$y_p = \frac{\int_{\Delta v} y I_{bv}(T)dv}{\int_{\Delta v} I_{bv}(T)dv}, \tag{18}$$

where y is a general notation representing absorption, scattering coefficients and single scattering albedo and y_p is the Planck-mean value in the sub-bands. The number of sub-bands N_b is found from a grid dependence test where less than 5% change is observed when using 2500 sub-bands or more.

Monte Carlo simulations are based on random sampling procedures so any practical results will have a non-zero variance associate with it. One measure of performance is to compute the variance of multiple runs, which can always be reduced by increasing the number of samples, but at the penalty of increasing computational

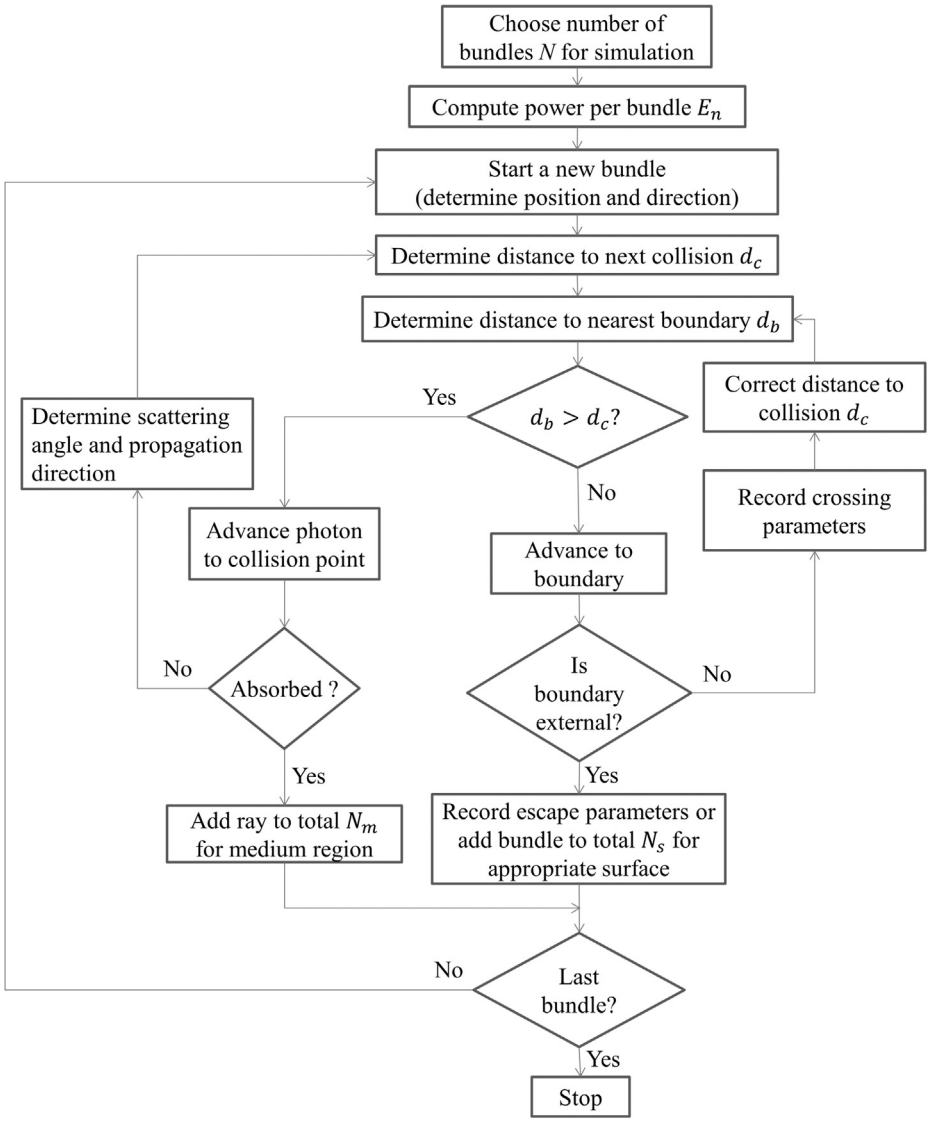

Fig. 4. Flow chart of Monte Carlo simulation procedure for forward collision-based approach.

time. Variance reduction techniques are used to improve performance while significantly reducing the required number of samples [37].

Biasing is a common technique for variance reduction. When source particles are sampled over space, energy, angle or time, some source particles may be more likely to contribute to a particular quantity of interest than others [40]. Traditional source biasing techniques enable the simulation of more source particles with reduced weights from more important regions [41]. In our case, the radiative transfer in some spectral bands (infrared atmospheric windows 800–1200 cm^{-1}, 2000–2300 cm^{-1} and 2400–2500 cm^{-1}) are more sensitive to optical properties of aerosols, so the contribution of anisotropic scattering effect is larger than that in other bands. The technique adopted here starts by choosing the modified (biased) probability distribution for bands in terms of their contribution to DLW radiative flux and anisotropic scattering effect, and then correcting the corresponding weight of each source particle by $w_{\text{biased}} \cdot p(x)_{\text{biased}} = w_{\text{unbiased}} \cdot p(x)_{\text{unbiased}}$, where w represents the weight while $p(x)$ is the probability distribution of the physical process being sampled. The sum of probability $p(x)$ is $\int p(x)_{\text{biased}}\, dx = \int p(x)_{\text{unbiased}}\, dx = 1$. Note that the total weight of source particles is also conserved. In our case, the unbiased value $p(x)$ is constant for all bands with same particle weight while biased probability distribution increases the number of bundle samples in atmospheric windows and decreases the weight of each bundle.

This variance reduction method successfully reduces computation time in the bands that do not contribute significantly to anisotropic scattering effects, and provides substantial improvements to the computational efficiency of the Monte Carlo simulations.

4. Net result based scaling rules

4.1. Model validation

Spectral comparisons of surface DLW flux densities between the Monte Carlo simulation and two-flux modeling results are shown in Fig. 5. Model results for verification are compared with the results from the Atmospheric and Environmental Research (AER) report for Case 27 (aerosol-free) in the Intercomparison of Radiation Codes in Climate Model (ICRCCM) program [42]. Despite of fluctuations caused by statistical nature of Monte Carlo method, the overall shape of the Monte Carlo simulation matches well with

the modeled profile. The absolute difference is smaller than 0.05 W cm m^{-2} for all wavenumbers.

4.2. The effect of anisotropic scattering

Fig. 5 also presents the difference of spectral DLW flux density between a highly forward or backward scattering atmosphere and an isotropic scattering atmosphere with dark-green bars and light-green bars, respectively. The spectral band between 750 cm^{-1} and 1400 cm^{-1} with high albedo and high Planck's emission are affected the most by the anisotropic scattering. Bands above 2000 cm^{-1} have large albedo but small Planck's emission, therefore their contributions are smaller.

As expected, when backward scattering is dominant ($e_g = -0.9$), the downwelling radiation flux is higher than the flux for isotropic medium, while when forward scattering is dominant ($e_g = 0.9$), the anisotropic flux is lower. This can be explained by the decrease of temperature and absorption coefficients with respect to altitude. For a backward scattering dominant medium, the DLW that is back-scattered from upwelling radiation emitted from lower layers would exceed the upward longwave radiation that is back-scattered from downwelling radiation emitted from upper layers, resulting an enhancement of downwelling flux. And the DLW is weakened by the forward scattering dominant medium in the similar way. For the considered model atmosphere with prescribed profiles [7], the broadband contribution of DLW from backward scattering is about 0.620 W m^{-2} and broadband forward scattering contribution is about −0.733 W m^{-2}.

4.3. The exponential relationship between the correction factor and the aerosol loading values

The radiative transfer equation (RTE) that describes the photon propagation through participating atmosphere is [43]:

$$\mu\frac{\partial I(\kappa,\mu)}{\partial\tau} + I(\kappa,\mu) = (1-\tilde{\rho})I_b(T) + \frac{\tilde{\rho}}{2} \times \int_{-1}^{1} P(\mu,\mu')I(\kappa,\mu')d\mu', \tag{19}$$

where $\mu = \cos\theta$ represents the zenith direction of the radiation ray (azimuthal symmetry is assumed); κ (cm^{-1}) is the extinction coefficient as the sum of absorption and scattering coefficients; $I(\kappa,\mu)$ and $I_b(T)$ (W m^{-2}) are the radiant intensity in the medium and blackbody radiant intensity, respectively; τ is the optical depth; $\tilde{\rho}$ is the single scattering albedo; T (K) is the temperature of the medium; μ' represents the scattered direction and $P(\mu,\mu')$ is the scattering phase function [8].

By introducing a source function j_v to represents photon emission and scattering, the radiative transfer Eq. (19) can be written in a simplified form

$$\frac{dI_v}{ds} = -\kappa_{e,v}I_v + j_v, \tag{20}$$

where I_v (W m^{-2} sr^{-1}) is the spectral intensity, $\kappa_{e,v} = \kappa_{a,v} + \kappa_{s,v}$ (cm^{-1}) is the extinction coefficient, s (m) is the path length.

The anisotropic effect shall be a function of single scattering albedo $\tilde{\rho}$ and asymmetry factor e_g of aerosols. A normalized optical depth is introduced to quantify $\tilde{\rho}$,

$$t^* = \frac{\kappa_s L}{\kappa_{s0} L}, \quad \tilde{\rho} = \frac{t^*\kappa_{s0,\mathrm{aer}}}{t^*\kappa_{s0,\mathrm{aer}} + t^*\kappa_{a0,\mathrm{aer}} + \kappa_{a,\mathrm{gas}}}, \tag{21}$$

where L is the thickness of the atmosphere and κ_{s0} is equivalent to AOD equals 0.1 at 500 nm at the surface.

Analogy to Eq. (20), the relationship between the anisotropic scattering effect $D(t^*)$ and the normalized optical path t^* for scattering is assumed to satisfy a first order ODE

$$\frac{dD(t^*)}{dt^*} = -\eta D(t^*) + c, \tag{22}$$

where $D(t^*) = (q^-_{\mathrm{ani}} - q^-_{\mathrm{iso}})/q^-_{\mathrm{ani}}$ is the anisotropic correction factor that quantifies the anisotropic scattering effect. The solution of the first order ODE is

$$D(t^*) = Ae^{-\eta t^*} + \frac{c}{\eta} \tag{23}$$

With the boundary condition $D(t^* = 0) = 0$, we have $A = -c/\eta$, then,

$$D(t^*) = -\frac{c}{\eta}\left(e^{-\eta t^*} - 1\right) \tag{24}$$

where coefficients c and η are functions of asymmetry factors e_g.

When the concentration of aerosols increases, more radiative cross section overlapping will occurs, then the addition of aerosols

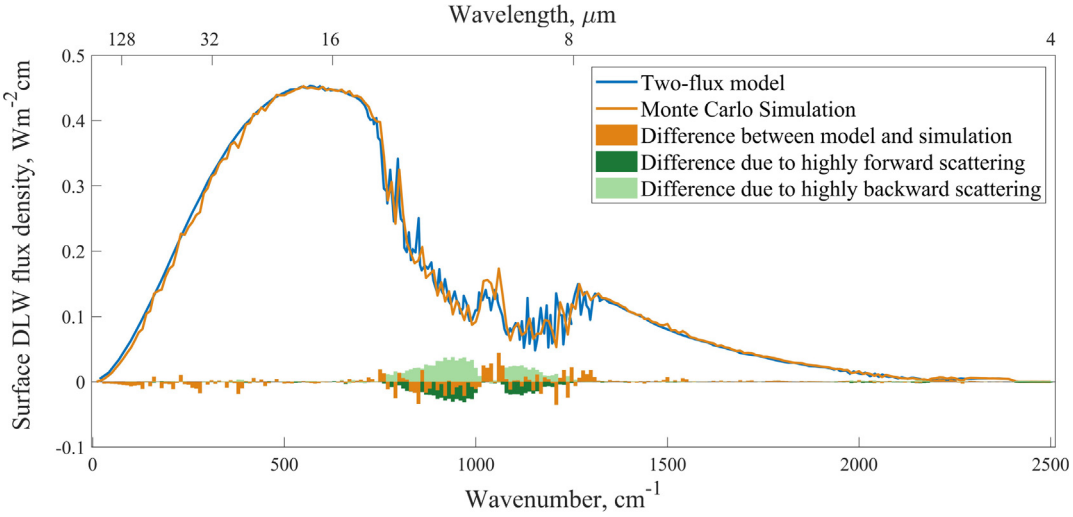

Fig. 5. Comparison of spectral surface DLW flux densities between Monte Carlo simulation (centrally averaged) and the results obtained from a two-flux model in [7].The differences of flux density due to anisotropic effects are also presented. Dark green bars and light green bars represent highly forward scattering case ($e_g = 0.9$) and highly backward scattering case ($e_g = -0.9$) respectively. (For interpretation of the references to colour in this figure legend, the reader is referred to the web version of this article.)

Table 5
Number of days in 2016 that t^* exceeded certain values for Beijing (China), Kanpur (India) and Banizoumbou (Niger).

City	$t^* \geqslant 10$	$t^* \geqslant 15$	$t^* \geqslant 20$	$t^* \geqslant 30$	Number of days in the dataset
Beijing	73	37	18	3	278
Kanpur	81	22	7	1	309
Banizoumbou	68	13	3	2	362

would contribute to smaller anisotropic scattering effect, following an exponential behaviour. The exponential behaviour is validated and the values of η and c are evaluated numerically in the following sections.

The anisotropic scattering effect of aerosols increases with increased aerosol concentrations t^*. In some regions of the world, the mean daily values of AOD are often as high as 3.0 (corresponds to $t^* = 30$), while the annual mean over the continent of United States is of the order of 0.1 (corresponds to $t^* = 1$). Table 5 shows a few cities and the number of days in 2016 for which t^* exceeded certain values [44]. For these urban areas, there are many days in a year when very high t^* values are recorded. Since evaluation of the anisotropic scattering effect is especially significant for these conditions, we then ranges t^* from 0 to 30 in the following analysis to cover the possible range of aerosol loadings.

4.4. The scaling rule for aerosols with varying asymmetry factors

Fig. 6 shows the effects of anisotropy $D(t^*, e_g)$ with respect to normalized optical depth t^* and asymmetry factor e_g. The internal mixing aerosol type is used with its spectral asymmetry factor set to vary from −1 to 1. Monte Carlo results obtained from both δ-M scaling and utilization of H-G phase function are presented. The correction factor $D(t^*, e_g)$ increases linearly with increasing asymmetry factor e_g for both backward and forward scattering conditions, as shown in Fig. 6(c). For $t^* < 5$, results from the δ-M approximation and from H-G phase function are identical, indicating that for low aerosol loadings, the δ-M approximation is sufficiently accurate that can be directly used in analytical models such as the two-flux models. For high aerosol loadings, δ-M approximation would underestimate DLW by 0.4% compared to H-G simulations for highly forward scattering cases (corresponds to around 1.2 W m^{-2}), then H-G phase function should be used for more precised results. For all cases considered, the anisotropy contributes to less than 2.0% error in surface DLW, as shown in Fig. 6 (a) and (b).

Fig. 6 (d) shows the relationship between $D(t^*, e_g)/e_g$ with respect to t^*, which can be fit using an exponential function as Eq. (24),

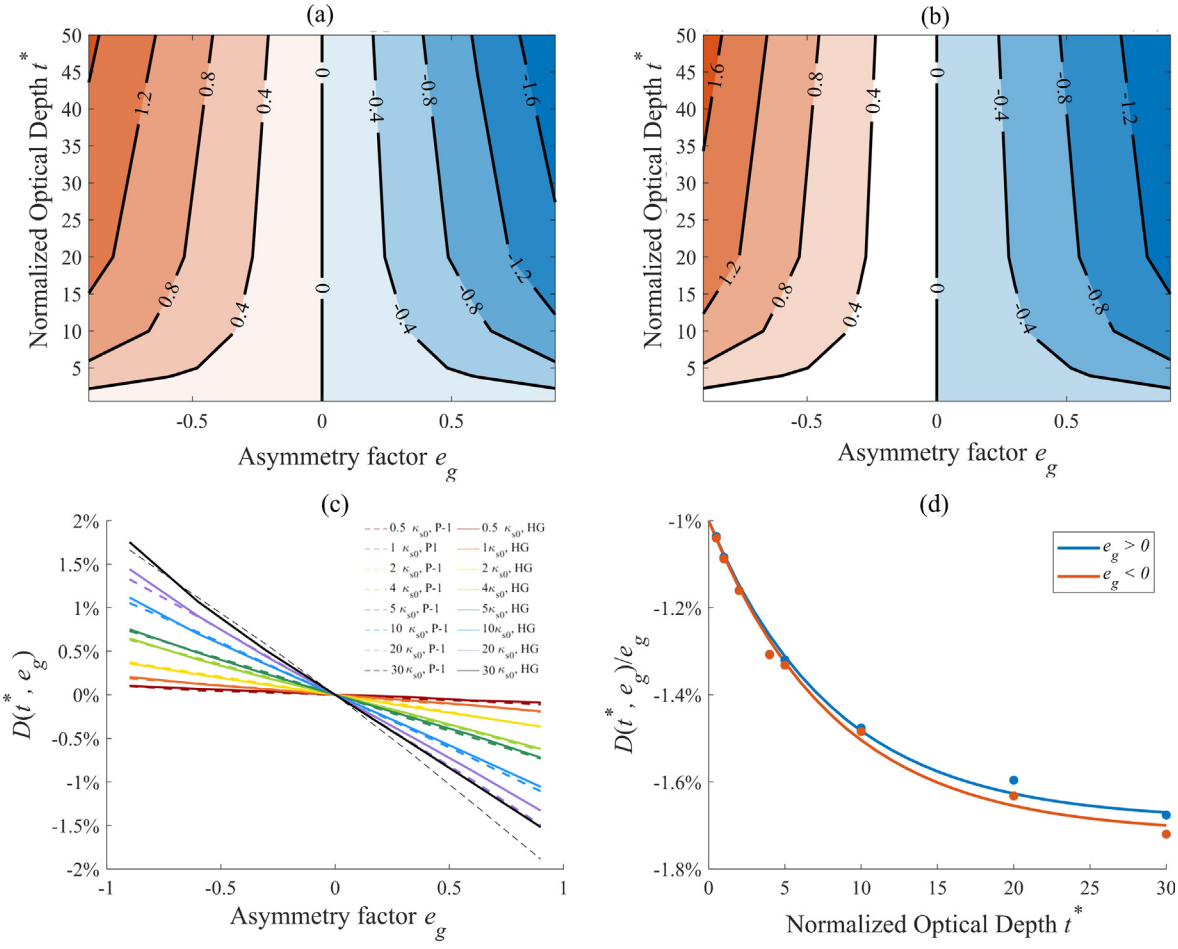

Fig. 6. Anisotropic correction factor $D(t^*, e_g)$ (%) with respect to normalized aerosol optical depth t^* and asymmetry factor e_g for (a) Monte Carlo δ-M approximation and (b) Monte Carlo H-G simulations. (c) Correction factor is a linear function of asymmetry factor. (d) $D(t^*, e_g)/e_g$ is an exponential function of t^* for both forward and backward scattering conditions.

Table 6
Parameters A, η, and $R^2$2 in Eq. (25) for different asymmetry factor range.

	A	η	R^2
$e_g \geq 0$	0.0179	0.1207	0.9913
$e_g < 0$	0.0169	0.1207	0.9924

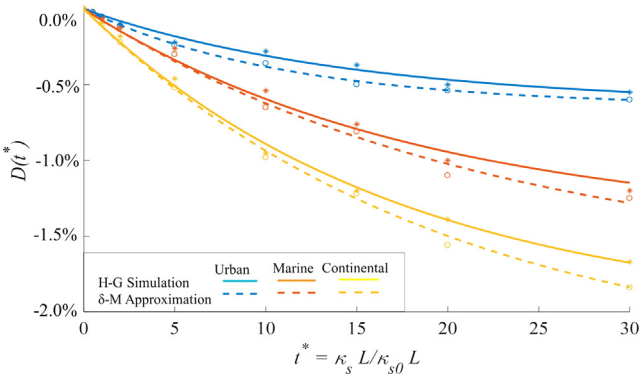

Fig. 7. Anisotropic correction factor with respected to normalized aerosol optical depth when RH = 70% for three types of aerosols. Symbols represent Monte Carlo simulation results while lines represent exponential fitting functions. Results obtained by using H-G phase functions and using δ-M approximation are plotted for comparison.

$$D(t^*, e_g) = -\frac{e_g A}{\eta}\left(e^{-\eta t^*} - 1\right) \tag{25}$$

The coefficients A and η are tabulated in Table 6 with R^2 values greater than 0.99.

When $t^* > 10$, the correction factor $D(t^*, e_g)/e_g$ becomes notably different for forward and backward scattering cases. Note that the correction factor $D(t^*, e_g)$ is regressed from the Monte Carlo simulations for the model atmosphere considered in this work. If substantially different temperature and constituent profiles are considered (especially aerosol profile), the coefficients for $D(t^*, e_g)$ may differ but the exponential relationship with respect to t^* and e_g holds, as derived in Section 4.3.

4.5. The scaling rule for different types of aerosols

Fig. 7 plots $D(t^*)$ with respect to normalized aerosol optical depth t^* for the three aerosol types: Urban, Marine and Continental aerosols, as described in Section 2.2, when ambient relative humidity is 70%. Monte Carlo simulation results using H-G phase function (star markers and solid lines) and using δ-M approximation (circle markers and dashed lines) are compared. The δ-M approximation deviates from H-G results when $t^* > 5$, overestimates the absolute value of anisotropic effects and its accuracy degrades with increased aerosol concentrations. Since aerosol anisotropic scattering effect is dominant by the aerosol optical properties in the atmospheric window band, continental aerosols with the highest absorption/scattering coefficients have the largest correction factor. Urban aerosols are the least affected by anisotropic scattering because of low values of e_g in the window band. The quantitative relationship between $D(t^*)$ and t^* are fit using an exponential expression using Eq. (24), and the aerosol-type-dependent coefficients c and η are tabulated in Table 7. The values of R^2 are greater than 0.99, verifying that $D(t^*)$ is an exponential function of t^* even when the types of aerosols are significantly different.

Since the optical properties of aerosols depend on the ambient relative humidity (refer to Section 2.2), here the sensitivity analysis of the correction factors to ambient relative humidity is performed. Not only the size distribution and refractive index of aerosols are

Table 7
Values of coefficients of c and η for different aerosol types. The R^2 for exponential fitting are also listed.

	H-G phase function			δ-M approximation		
	c	η	R^2	c	η	R^2
Urban aerosol	3.8×10^{-4}	0.05241	0.9916	4.7×10^{-4}	0.05811	0.9904
Marine aerosol	7.8×10^{-4}	0.05743	0.9911	8.8×10^{-4}	0.06204	0.9914
Continental aerosol	1.24×10^{-3}	0.06515	0.9978	1.32×10^{-3}	0.06374	0.9972

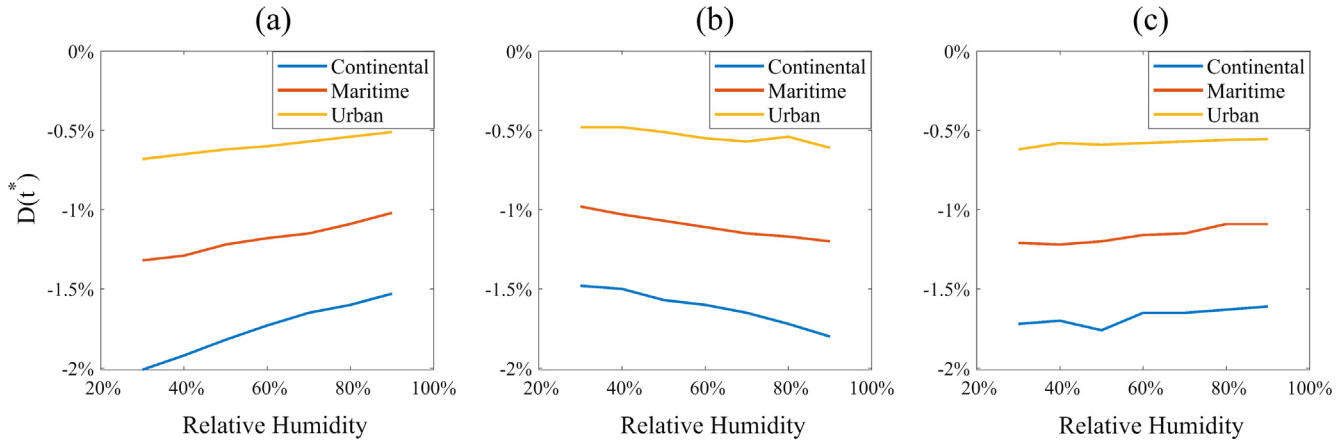

Fig. 8. Sensitivity of the anisotropic correction factors to ambient relative humidity when $t^* = 30$ under three scenarios: (a) hold aerosol optical properties constant (as for RH = 70% condition) and change absorption coefficient of atmospheric gases due to changing water vapor content. (b) hold atmospheric absorption coefficient constant (as for RH = 70% condition) and vary aerosol optical properties. and (c) the combined effects from scenarios (a) and (b).

functions of ambient relative humidity [23], but also the absorption coefficients of atmospheric layers are functions of relative humidity because water vapor is the main participator. Fig. 8 shows the anisotropic correction factor $D(t^*)$ with respect to ambient relative humidity for very high aerosol loadings ($t^* = 30$) under three scenarios. Scenario (a) shows the effects of varying absorption coefficients of the atmospheric layers due to varying water vapor content, assuming that aerosol optical properties are unchanged (optical properties of aerosol at 70% relative humidity is used). The negative correction factors increase with increasing values of relative humidity, because the aerosol forcing is less obvious when more water vapor is present. Scenario (b) shows the effects of varying aerosol optical properties due to varying relative humidity, assuming that the absorption coefficients of the atmospheric layers are unchanged ($\kappa_{a,\mathrm{gas}}$ at 70% relative humidity is used). The negative correction factors decrease with increasing values of relative humidity, because wet aerosols contributes more to the radiative forcing and have stronger anisotropic effects. Scenario (c) shows the combined effects of scenarios (a) and (b), where the two opposite effects cancel, leaving the correction factor not sensitive to the relative humidity, even for the considered high aerosol loadings ($t^* = 30$).

5. Conclusions

A comprehensive Monte Carlo model is used to evaluate quantitatively the accuracy of the isotropic scattering assumption in calculating surface downwelling longwave irradiance (DLW) during clear skies.

The atmosphere is modeled as an 18-layer, plane parallel system with standard temperature and concentration profiles. The absorption, scattering coefficients and asymmetry factors of aerosols are modeled using Mie theory equations, and aerosol scattering is modeled using Henyey-Greenstein phase functions. We use a direct Monte Carlo (MC) method as a baseline anisotropic radiative transfer model that requires no directional assumptions (e.g. diffuse medium and isotropic scattering in two-flux model) to compute accurate values of the downwelling longwave radiation (DLW) for different aerosol concentrations and properties. The present work proposes two scaling rules that correct the surface DLW calculated by assuming isotropic scattering and diffuse radiative properties.

The first scaling rule is input based, and is used to scale the input optical properties such as extinction coefficient and the single scattering albedo values as done in the widely used δ-M approximation. The second scaling rule is net result based. The net result based method scales the output surface DLW based on the results from detailed MC simulations. Henyey-Greenstein phase functions are used to approximate Mie scattering equations. The latter method and is presumed to be more accurate than the former. The latter net result based approach is also substantially more expensive computationally, and is used here as a benchmark for the validity of the δ-M approximation.

The correction factor $D(t^*) = (q^-_{ani} - q^-_{iso})/q^-_{ani}$ correlates exponentially with the normalized aerosol optical depth t^*, i.e. $D(t^*) = -c/\eta(e^{-\eta t^*} - 1)$. Detailed simulations were performed for both aerosol-type-neutral and aerosol-type-dependent cases. For aerosol-type-neutral cases, D is also a function of asymmetry factor e_g, and the coefficient c is expressed as $c = e_g A$. Regression coefficients A and η are provided for both backward and forward scattering cases. More generally, the anisotropic effect is dependent on aerosol composition. For aerosol-type-dependent cases, the regression coefficients c and η for three types of aerosols (urban, continental and maritime) are also investigated. For all cases under consideration, the correction factor D is an exponential function of t^*, revealing the underlying nature of the anisotropic scattering correction. The δ-M approximation is found to be accurate when $t^* < 5$ (equivalent to surface AOD < 0.5). For values of t^* of the order of 30 (equivalent to surface AOD equal to 3), the error incurred by the isotropic scattering assumption is of the order of 2.0% ($\approx$5 W m^{-2}). The relative offset is highest for continental aerosols and lowest for urban aerosols, but the much higher values of AOD observed in urban areas contribute to a more significant correction in these cases, and may represent a relevant bias in DLW values for cities such as Beijing and Kanpur. The influence of relative humidity on the correction factor is found to be negligible even at very high aerosol loads.

In summary, this work proposes two scaling rules to expedite surface DLW calculations by means of corrections to the isotropic scattering assumptions. Optimal scaling rules for urban, continental and marine aerosols are reported. The input-scaling approach (δ-M approximation) is generally accurate for relatively low aerosol loading values observed in non-urban areas, while the proposed net-result-based scaling is valid for all values of aerosol loading, including high aerosol urban areas, and rural and urban areas affected by large-scale fire pollution.

Conflict of interest

The authors declared that there is no conflict of interest.

References

[1] P. Berdahl, M. Martin, F. Sakkal, Thermal performance of radiative cooling panels, Int. J. Heat Mass Transf. 26 (1983) 871–880.
[2] A. Yoshida, T. Kunitomo, One-dimensional simulation of the thermal structure of urban atmospheres, Int. J. Heat Mass Transf. 29 (1986) 1041–1049.
[3] M. Li, Y. Jiang, C.F.M. Coimbra, On the determination of atmospheric longwave irradiance under all-sky conditions, Sol. Energy 144 (2017) 40–48.
[4] M. Li, C.F.M. Coimbra, On the effective spectral emissivity of clear skies and the radiative cooling potential of selectively designed materials, Int. J. Heat Mass Transf. 135 (2019) 1053–1062.
[5] D.J. Yang, Z.F. Yuan, P.H. Lee, H.M. Yin, Simulation and experimental validation of heat transfer in a novel hybrid solar panel, Int. J. Heat Mass Transf. 55 (2012) 1076–1082.
[6] E. Shahraeeni, D. Or, Quantification of subsurface thermal regimes beneath evaporating porous surfaces, Int. J. Heat Mass Transf. 54 (2011) 4193–4202.
[7] M. Li, Z. Liao, C.F.M. Coimbra, Spectral model for clear sky atmospheric longwave radiation, J. Quant. Spectrosc. Radiat. Transf. 209 (2018) 196–211.
[8] H. Lee, R.O. Buckius, Scaling anisotropic scattering in radiation heat transfer for a planar medium, J. Heat Transf. 104 (1982) 68–75.
[9] B.H.J. McKellar, M.A. Box, The scaling group of the radiative transfer equation, J. Atmos. Sci. 38 (26) (1981) 1063–1068.
[10] J.H. Joseph, W.J. Wiscombe, J.A. Weinmann, The delta-Eddington approximation for radiative flux transfer, J. Atmos. Sci. 33 (1976) 2452–2459.
[11] J.F. Potter, The delta function approximation in radiative transfer theory, J. Atmos. Sci. 27 (1970) 943–949.
[12] W.J. Wiscombe, The delta-M method: rapid yet accurate radiative flux calculations for strongly asymmetric phase functions, J. Atmos. Sci. 34 (1977) 1408–1422.
[13] Z. Guo, S. Maruyama, Scaling anisotropic scattering in radiative transfer, Int. Commun. Heat Mass Transf. 26 (7) (1999) 997–1007.
[14] L.A. Dombrovsky, W. Linpinski, A combined p_1 and Monte Carlo model for multidimensional radiative transfer problems in scattering media, Comput. Therm. Sci. 2 (26) (2010) 549–560.
[15] J. Heino, S. Arridge, J. Sikora, E. Somersalo, Anisotropic effects in highly scattering media, Phys. Rev. E 68 (2003) 031908.
[16] S. Manabe, R.F. Strickler, Thermal equilibrium of the atmosphere with a convective adjustment, J. Atmos. Sci. 21 (4) (1964) 361–385.
[17] G.P. Anderson, S.A. Clough, F.X. Kneizys, J.H. Chetwynd, E.P. Shettle, AFGL atmospheric constituent profiles (0 to 120 km), Tech. rep., Air Force Geophysics Laboratory, 1986.
[18] I.E. Gordon, L.S. Rothman, C. Hill, R.V. Kochanov, Y. Tan, P.F. Bernath, M. Birk, V. Boudon, A. Campargue, K. Chance, The HITRAN2016 molecular spectrospopic data base, J. Quant. Spectrosc. Radiat. Transf. 203 (2017) 3–69.
[19] M. Cherkaoui, J.-L. Dufresne, R. Fournier, J.-Y. Grandpeix, A. Lahellec, Monte Carlo simulation of radiation in gases with a narrow-band model and a net-exchange formulation, ASME J. Heat Transf. (1996) 401–407.
[20] H. Yu, M. Chin, D.M. Winker, A.H. Omar, Z. Liu, C. Kittaka, T. Diehl, Global view of aerosol vertical distributions from CALIPSO lidar measurements and GOCART simulations: Regional and seasonal variations, J. Geophys. Res.: Atmos. 115 (2010).

[21] Q. Xu, H. Wei, R. Rao, H. Hu, Simultaneous determination of aerosol optical thickness and exponent of Junge power law from satellite measurements of two near-infrared bands over the ocean, Opt. Express 15 (8) (2007) 5227–5236.
[22] C. Pilinis, S.N. Pandis, J.H. Seinfeld, Sensitivity of direct climate forcing by atmospheric aerosols to aerosol size and composition, J. Geophys. Res. 100 (D9) (1995) 18739–18754.
[23] D. Lubin, S.K. Satheesh, G. McFarquar, A.J. Heymsfield, Longwave radiative forcing of Indian ocean tropospheric aerosol, J. Geophys. Res. - Atmos. 107 (D19) (2002), INX2 3–1-INX2 3–13.
[24] A.A. Kokhanovsky, Aerosol Optics: Light Absorption and Scattering by Particles in the Atmosphere, Praxis Publishing, Chichester, UK, 2008.
[25] G.A. DAlmeida, P. Koepke, E.P. Shettle, Atmospheric Aerosols: Global Climatology and Radiative Characteristics, A.DEEPAK Publishing, Hampton, VA, USA, 1991.
[26] E.F. Vermote, D. Tanre, J.L. Deuze, M. Herman, J.J. Morcrette, Second simulation of the satellite signal in the solar spectrum, 6S: an overview, IEEE Trans. Geosci. Remote Sens. 35 (1997) 675–686.
[27] E.M. Patterson, D.A. Gillette, Commonalities in measured size distributions for aerosol having a soil-derived component, J. Geophys. Res. 82 (15) (1977) 2074–2082.
[28] Y.J. Kim, H. Sievering, J.F. Boatman, Airborne measurement of atmospheric aerosol particles in the lower troposphere over the central United States, J. Geophys. Res. 93 (D10) (1988) 12631–12644.
[29] J. Blanchet, R. List, Estimation of optical properties of arctic haze using a numerical model, Atmos. Ocean 21 (4) (1983) 444–465.
[30] C. Tomasi, S. Fuzzi, A. Kokhanovsky, Atmospheric Aerosols: Life Cycles and Effects on Air Quality and Climate, 18th ed., John Wiley and Sons, Cambridge, MA, 2016.
[31] D. Forgan, An introduction to Monte Carlo radiative transfer, Tech. rep., Institute for Astronomy Royal Observatory Edinburgh, 2009.
[32] M.F. Modest, Radiative Heat Transfer, third ed., Academic Press, Cambridge, MA, 2013.
[33] B.A. Whitney, Monte Carlo radiative transfer, Bull. Astron. Soc. India 39 (2011) 101–127.
[34] J.T. Farmer, J.R. Howell, Monte Carlo prediction of radiative heat transfer in inhomogeneous, anisotropic, nongray media, J. Thermophys. Heat Transf. 8 (1) (1994) 133–139.
[35] E.D. Cashwell, C.J. Everett, A Practical Manual of the Monte Carlo Method for Random Walk Problems, Pergamon Press, Los Alamos, NM, 1959.
[36] D. Toublanc, Henyey-Greenstein and Mie phase functions in Monte Carlo radiative transfer computations, Appl. Opt. 35 (18) (1996) 3270–3274.
[37] O.N. Vassiliev, Monte Carlo Methods for Radiation Transport: Fundamentals and Advanced Topics, Springer International Publishing, Berlin, 2017.
[38] L.L. House, L.W. Avery, The Monte Carlo technique applied to radiative transfer, J. Quant. Spectrosc. Radiat. Transf. 9 (1969) 1579–1591.
[39] A. Maurente, F.H.R. França, A multi-spectral energy bundle method for efficient Monte Carlo radiation heat transfer computations in participating media, Int. J. Heat Mass Transf. 90 (2015) 351–357.
[40] S.A. Dupree, S.K. Fraley, Monte Carlo Primer: A Practical Approach to Radiation Transport, Kluwer Academic/Plenum Publishers, New York, NY, 2002.
[41] A. Haghighat, J.C. Wagner, Monte Carlo variance reduction with deterministic importance functions, Prog. Nucl. Energy 42 (1) (2003) 25–53.
[42] U.S. Department of Energy, ICRCCM infrared (clear-sky) line-by-line radiative fluxes (DB-1002), 2017. <http://cdiac.ornl.gov/ndps/db1002.html>.
[43] S. Chandrasekhar, Radiative Transfer, Oxford University Press, Oxford, UK, 1950.
[44] NASA Goddard Space Flight Center, Aerosol robotic network, 2016. <https://aeronet.gsfc.nasa.gov/new_web/aerosols.html> (accessed: 2018-06-10).